Journal of Catalysis **207,** 213–223 (2002)
doi:10.1006/jcat.2002.3516, available online at http://www.idealibrary.com on IDEAL®

Cerium Containing MCM-41-Type Mesoporous Materials and their Acidic and Redox Catalytic Properties

S. C. Laha,* P. Mukherjee,* S. R. Sainkar,† and R. Kumar*,[1]

**Catalysis and †Physical Chemistry Division, National Chemical Laboratory, Pune 411 008, India*

Received June 15, 2001; revised November 19, 2001; accepted January 3, 2002

The syntheses of cerium containing MCM-41 mesoporous molecular sieves (Ce–MCM-41) were carried out using different hydrothermal methods. However, the Ce–MCM-41 samples were mainly prepared by refluxing the gel mixture at atmospheric pressure under stirring (∼600 rpm). For comparison, the syntheses were also carried out in autoclave under autogeneous pressure both in static and in stirring conditions. Powder X-ray diffraction (XRD), N_2 adsorption, diffuse reflectance UV–visible (UV–vis) spectroscopy, IR spectroscopy, solid state magic-angle spinning nuclear magnetic resonance spectroscopy, scanning electron microscopy, energy-dispersive X-ray spectrometry (EDX), transmission electron microscopy and thermogravimetric analyses of the samples reveal that well-ordered MCM-41-type mesoporous materials were prepared and Ce is incorporated presumably into the framework position and/or into the walls of silica matrix of MCM-41 structure. The EDX analyses of the samples confirm the presence of Ce in the Ce–MCM-41 samples. Typical XRD patterns of MCM-41-type hexagonal structures and high BET surface areas (983–1414 m^2 g^{-1}) with isotherms of type IV of these materials indicate the presence of hexagonal mesopores in the samples. The presence of a strong absorption band centered at ca. 300 nm and the absence of any absorption band at ca. 400 nm in the diffuse reflectance UV–vis spectra indicate the presence of tetra-coordinated cerium in the silica network of Ce–MCM-41 samples. The Ce–MCM-41 samples are active as catalysts for vapor-phase dehydration of cyclohexanol to cyclohexene and hydroxylation of 1-naphthol with aqueous H_2O_2 and *tert*-butyl hydroperoxide.

Key Words: **synthesis of MCM-41; cerium; catalytic activity; dehydration of cyclohexanol; hydroxylation of 1-naphthol.**

INTRODUCTION

The advantage of zeolites and related molecular sieves as heterogeneous catalysts over the homogeneous ones is that they avoid contamination of the effluents, which are becoming increasingly difficult to dispose of. Zeolites and related molecular sieves are largely being used for various catalytic applications because of their unique structural and textural properties. However, the pore size limitations of the microporous zeolites (<15 Å) limited the use of bigger molecules for catalytic conversions inside the zeolitic channels. The major breakthrough came when Mobil reported the successful synthesis of mesoporous M41S materials in 1992 (1, 2). Since then, hexagonal mesoporous silica (HMS) (3), mesoporous aluminophosphate (4), different types of mesoporous metallophosphates (5, 6), and other mesoporous molecular sieves such as FSM-16 (7), KIT-1 (8), and so forth, were also synthesized successively. Out of these materials, M41S materials were studied extensively. These materials were synthesized using self-assembled molecular aggregates or supramolecular assemblies as structure-directing agents. Everything from synthesis to the potential applicability of these materials in catalysis have been reviewed by several authors (9–12). Among the other members of the M41S family, the synthesis and catalytic applications of MCM-41-type mesoporous materials have been investigated extensively. This material exhibits hexagonal array of unidimensional mesopores, the diameter of which can be tuned in the range between 20 and 100 Å with a narrow pore size distribution, through the proper choice of surfactant as the template, auxiliary chemicals, and reaction conditions.

The incorporation of divalent (Co, Zn), trivalent (B, Al, Ga, Cr, Fe), and tetravalent (Ti, V, Mn, Sn, Zr, etc.) transition and nontransition metal ions in the silica network of MCM-41 materials has been reported (13). Recently, a brief report about cerium silicate analogues of MFI, BEA, and MTW was published (14). Due to size incompatibility between lanthanide and Si^{4+} ions, which will produce longer ≡Si–O–Ce≡ bonds, causing large bond-angle strain in Ce-substituted silica network, the incorporation of Ce in microporous metallosilicate molecular sieves is expected to be rather difficult. However, the incorporation of Ce into the framework of MCM-41 is expected to be easier because of the greater flexibility of the silica network. Further, the incorporation of Ce, an early member of lanthanides, in the MCM-41 silica network is expected to impart dual catalytic activity in heterogeneous acid as well as redox catalysis.

Accordingly, we now report on the detailed synthesis, characterization, and catalytic properties of cerium

[1] To whom correspondence should be addressed. Fax: +91-20-5893761/5893355. E-mail: rajiv@cata.ncl.res.in.

0021-9517/02 $35.00

containing MCM-41-type mesoporous molecular sieves. The environment of the cerium (Ce^{4+}) cation in the Ce–MCM-41 molecular sieves was determined by different methods and the obtained materials were tested as catalysts for vapor-phase dehydration of cyclohexanol and hydroxylation of 1-naphthol with aqueous H_2O_2 and TBHP.

EXPERIMENTAL

Materials

The syntheses of pure siliceous MCM-41 and several Ce-containing MCM-41 samples were carried out using fumed silica (Sigma, USA), a 25 wt% aqueous solution of tetramethylammonium hydroxide (TMAOH, Loba Chemie, India), ceric sulfate (Loba Chemie, India), and cetyltrimethylammonium bromide (CTMABr, Loba Chemie, India).

Synthesis

The hydrothermal syntheses were mainly carried out under reflux conditions at atmospheric pressure (R-series). However, the syntheses were also carried out in an autoclave under autogeneous pressure in stirring (P-series) as well as in static conditions (A-series). The molar gel compositions of the synthesis gels were 1 $SiO_2 : x CeO_2 : 0.30$ TMAOH : 0.25 CTMABr : 125 H_2O, where $x = 0$, 0.00625, 0.0125, 0.025, and 0.05.

In a typical synthesis of a Ce–MCM-41 sample, 3.0 g of fumed silica was slowly added to 5.47 g of TMAOH (25 wt%) in 10.0 g of water under vigorous stirring. Subsequently, an aqueous solution of ceric sulfate (0.505 g dissolved in 10.0 g of water) was added followed by the addition of 4.55 g of CTMABr dissolved in 30.0 g of water. The remaining 58.4 g of water was added and the stirring was continued for 15 min. Finally, the synthesis gel was taken in a glass flask (250-ml capacity) and refluxed for 48 h under stirring. The materials thus obtained were filtered, washed thoroughly first with deionized water and then with acetone, and dried at 353 K. All the samples were calcined at 813 K for 8 h in the presence of air. Ce–MCM-41 samples with Si/Ce ratios of 160, 80, 40, and 20 were prepared under reflux conditions. Ce–MCM-41 samples with Si/Ce = 40 were also prepared in an autoclave under autogeneous pressure in static conditions as well as in stirring conditions (Parr reactor) at 200 rpm both at 373 K for 48 h. The Ce-impregnated MCM-41 (Si/Ce = 20), Ce-exchanged MCM-41, and an amorphous physical mixture of silica and ceria (Si/Ce = 20) were also prepared for comparison purposes. All the samples were a light yellow color.

Characterization

The samples were characterized using powder X-ray diffraction (XRD), surface area measurements, diffuse reflectance UV–visible (UV–vis) spectroscopy, Fourier transform infrared (FTIR) spectroscopy, solid state magic-angle spinning (MAS) nuclear magnetic resonance (NMR), scanning electron microscopy (SEM), energy-dispersive X-ray analysis (EDX), transmission electron microscopy (TEM), and thermogravimetric analysis (TG-DTA).

The powder X-ray diffractograms of as-synthesized and calcined samples were recorded on a Rigaku Miniflex diffractometer with CuK_α radiation between 1.5 and 10° (2θ) with a scanning rate of 1°/min. The specific surface area, pore size, and pore volume of the calcined samples were determined by BET method from N_2 adsorption isotherms at 77 K using a Coulter instrument (Omnisorb 100 CX).

The diffuse reflectance UV–vis spectra were recorded in the 200- to 600-nm range with a Shimadzu UV-2101 PC spectrometer equipped with a diffuse reflectance attachment using $BaSO_4$ as a reference. The FTIR spectra were obtained in the 400- to 4000-cm^{-1} range on a Shimadzu FTIR-8201 PC (in Nujol using a KBr disk technique).

The solid state MAS NMR spectra were recorded on a Bruker MSL 300 NMR spectrometer. The resonance frequencies of ^{13}C and ^{29}Si were 75.5 and 59.6 MHz, respectively. The finely powdered samples were placed in 7.0-mm zirconia rotors and spun at 2.5–3.5 kHz. The chemical shifts were determined using adamantane ($\delta = 28.7$ ppm from TMS) and tetraethyl orthosilicate ($\delta = -82.4$ ppm from TMS) as the reference compounds for ^{13}C and ^{29}Si, respectively.

The SEM micrographs of the calcined samples were obtained in a Leica Stereoscan 440. TEM was preformed on a JEOL JEM-1200EX instrument with 100 kV of acceleration voltage to probe the mesoporosity of the MCM-41 samples. The metal content of the calcined samples was determined by EDX analyses with Kevex equipment attached to a Jeol JSM-5200 scanning microscope. The thermogravimetric analyses were carried out on a Setaram TG-DTA92 under a flow of air (2.5 L/h) at a heating rate of 10 K/min between 298 and 1000 K.

Catalytic Reactions

The catalytic reaction of dehydration of cyclohexanol was carried out in a fixed-bed down-flow reactor. The Ce–MCM-41 samples were pretreated at 673 K for 1 h in a flow of N_2 gas. Cyclohexanol was fed into the catalyst bed at 473 K using air as the carrier gas. After 1 h, the product was collected and analyzed by gas chromatography (GC). The conversion of cyclohexanol was calculated from the amount of cyclohexene formed.

To test the oxidative catalytic properties of Ce–MCM-41 samples, hydroxylation of 1-naphthol was carried out using 45 wt% aqueous H_2O_2 and 70 wt% aqueous TBHP as oxidants. The mixture of 1-naphthol, oxidant, and acetonitrile as solvent was added to the solid Ce–MCM-41 samples and the reaction mixture was heated for 12 h at a constant

temperature of 353 K under stirring. After the reaction, the reaction mixture was cooled to room temperature, and the organic layer was separated by centrifugation and/or by extraction with dichloromethane and then analyzed by Shimadzu 17A series gas chromatograph using a capillary column (HP 101 methyl silicone fluid, with 50-m-long, 0.2-mm-inner diameter, 0.2-μm-thick coated film). Selected samples were also analyzed by GCIR (Perkin Elmer, GC-IR 2000) and GCMS (Shimadzu, GCMS-QP 2000A) to identify the products.

RESULTS AND DISCUSSION

Powder X-Ray Diffraction

The powder X-ray diffractograms of as-synthesized Si–MCM-41 and Ce–MCM-41 samples with different Si/Ce ratios along with the Ce-exchanged MCM-41 sample are shown in Fig. 1. The well-defined XRD patterns may be indexed on the basis of four Bragg peaks, which can be distinguished in hexagonal lattice symmetry, characteristic of MCM-41 structure. A prominent peak for $hkl = 100$ as well as weaker peaks for $hkl = 110$, 200, and 210 were observed in the as-synthesized and the calcined samples. The d_{100} values are given in Table 1 along with the corresponding unit cell parameter (a_0) of different MCM-41 samples, calculated from the peak with $hkl = 100$ using the equation $a_0 = 2d_{100}/\sqrt{3}$. A slight increase in the d-values and unit-cell parameters is observed on incorporation of cerium and it increases with increasing cerium content. The increase in unit-cell parameter on Ce incorporation is probably due to the larger size of Ce^{4+} compared to Si^{4+}. Similar observations were also reported by earlier workers with different metal ions incorporated into MCM-41 (13). Therefore, it may be inferred that most of the Ce is incorporated into the framework position and/or walls of silica network of MCM-41. However, a gradual loss of long-range ordering is observed with increasing incorporation of Ce in the Ce–MCM-41samples. This is probably due to an increasing number of defect sites and bond strain in these materials, as evidenced by the decreasing intensities of the [100] peak as well as the higher angle peaks. Finally, at very high Ce loading (Si/Ce $\leq$10), amorphous material is obtained. Loss of long-range ordering is also observed for the Ce-exchanged MCM-41 sample.

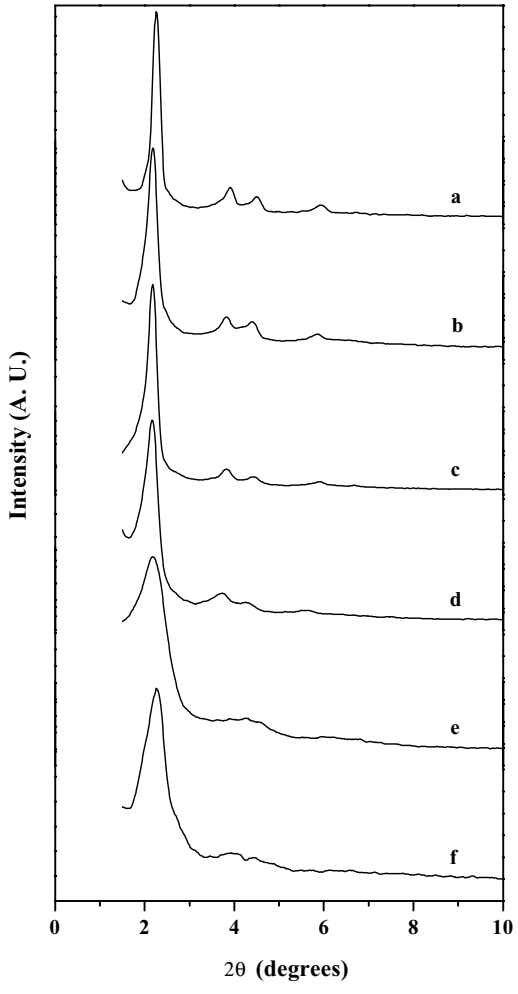

FIG. 1. X-ray diffraction patterns of as-synthesized (a) Si–MCM-41, (b) Ce–MCM-41-R-160, (c) Ce–MCM-41-R-80, (d) Ce–MCM-41-R-40, (e) Ce–MCM-41-R-20, and (f) Ce-exchanged MCM-41.

TABLE 1

Results of Elemental Analysis, d_{100} Spacing, and Unit Cell Parameter (a_0) of *M*–MCM-41 (M = Si and Ce) Samples

Sample[a]	$(Si/Ce)_{gel}$	$(Si/Ce)_{solid}$	d_{100} (Å)	a_0 (Å)
Si–MCM-41	—	—	38.2	44.1
Ce–MCM-41-R-160[b]	160	159.6	39.0	44.9
Ce–MCM-41-R-80	80	80.9	39.4	45.5
Ce–MCM-41-R-40	40	40.8	40.3	46.5
Ce–MCM-41-A-40	40	40.6	40.1	46.1
Ce–MCM-41-P-40	40	40.9	40.2	46.3
Ce–MCM-41-R-20	20	20.8	40.8	47.1
Ce-Ex–MCM-41[c]	—	44.1	38.0	43.9
Ce-Im–MCM-41-20[d]	20	20.1	38.0	43.9
SiO_2–CeO_2-20[e]	20	20.2	—	—

[a] R, A, and P denote samples synthesized under reflux conditions with stirring, in an autoclave under static conditions, and in a Parr autoclave with stirring, respectively.
[b] Numbers denote Si/Ce molar ratio in gel.
[c] Ce-exchanged MCM-41 sample.
[d] Ce-impregnated MCM-41 sample.
[e] Mixture of silica and ceric oxide.

N_2 Adsorption

The porosity of the MCM-41 samples was evaluated by N_2 adsorption isotherms. Figure 2 shows the N_2 adsorption–desorption isotherm and the corresponding pore size distribution curve (inset) for the Ce–MCM-41-R-40 sample.

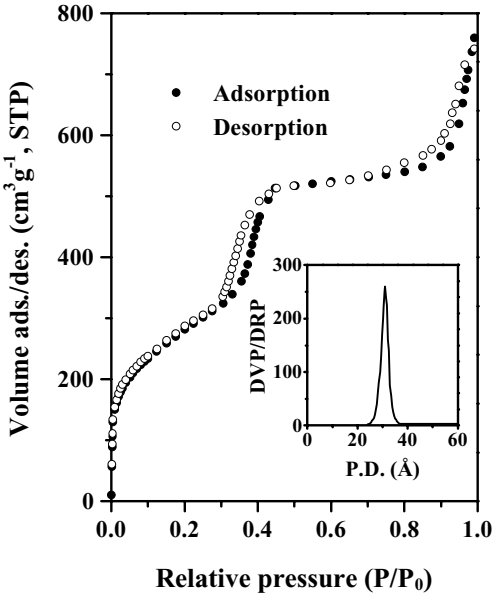

FIG. 2. Nitrogen adsorption–desorption isotherm and pore size distribution (inset) for Ce–MCM-41-R-40.

All the samples showed isotherms of type IV having inflection around $P/P_0 = 0.3$–0.45, characteristic of MCM-41 type ordered mesoporous materials. The samples exhibit complementary textural- and framework-confined mesoporosity, as evidenced by the presence of two separate, well-expressed hysterisis loops. One is in the $P/P_0 = 0.3$–0.45 region indicative of framework-confined mesopores and the other one is at $P/P_0 \geq 0.8$, corresponding to capillary condensation in the interparticle pores (15). The position of inflection in the $P/P_0 = 0.3$–0.45 region depends on the diameter of the mesopores and its sharpness indicates the uniformity of the narrow pore size distribution (16). It has also been observed that the point of inflection shifts toward higher relative pressure (P/P_0), with an increase in the Ce content of the Ce–MCM-41 samples indicating an increase in the pore size. The specific BET surface area, average pore diameters calculated from a N_2 adsorption isotherm using the BJH model, and specific pore volume for the MCM-41 samples are presented in Table 2. However, it is pertinent to mention that in general, it is agreed that the average pore size distribution calculated by the BJH method, using the Kelvin equation for nonintersecting cylindrical pores, as in MCM-41-type materials, underestimates the size of pores and, therefore, the KJS procedure which is based on a corrected Kelvin equation for hexagonal materials (17), is better. Nevertheless, the reported trend in the pore diameters of different MCM-41 samples is expected to be in conformity with the actual ones.

It has been observed that the BET surface area gradually decreases with an increase in the Ce-content of Ce–MCM-41 samples. However, the average pore diameters show an increasing trend with increasing Ce content of the samples. It may be inferred that the increase in pore size with Ce-incorporation is due to a larger size of Ce^{4+} compared to Si^{4+}. The decrease in surface area for the Ce-exchanged MCM-41 sample can be attributed to the loss in long-range ordering, as also seen in the XRD pattern. In the case of the Ce-exchanged MCM-41 sample, the increase in wall thickness and the decrease in pore size may be due to deposition of cerium species on the pore surface of cylindrical channels of MCM-41. However, the data presented in Table 2 show that the framework thickness (FWT), calculated by subtracting pore diameter by a_0, of different Ce-containing MCM-41 and purely siliceous MCM-41 samples is comparable and does not increase with increasing Ce content. Although, the unit cell parameter (a_0) increases with the increasing incorporation of Ce, as in other heterometal ions, which are larger than Si^{4+} ions (13, 18, 19), the pore diameter was also found to increase slightly, leading to a comparable FWT of different Ce–MCM-41 as well as Si–MCM-41 samples. Similar observations were made in the case of Sn–MCM-41 (19). The defect site may influence the a_0 or pore diameter or both, depending on their density and nature. Hence, we have not found any unambiguous correlation between the content of Ce and FWT in our present studies.

Diffuse Reflectance UV–vis Spectroscopy

The diffuse reflectance UV–vis spectroscopy is known to be a very sensitive probe for the identification and characterization of metal ion coordination and its existence in the framework and/or in the extraframework position of metal containing zeolites. The diffuse reflectance UV–vis spectra of calcined Ce–MCM-41 samples, given in Fig. 3,

TABLE 2

Nitrogen Sorption Pore Diameter, Pore Volume, FWT, and BET Surface Area of *M*–MCM-41 (*M* = Si and Ce) Samples

Sample[a]	Pore diameter (Å)	Pore volume ($cm^3\ g^{-1}$)	FWT[b] (Å)	BET SA ($m^2\ g^{-1}$)
Si–MCM-41	28.6	1.08	15.5	1414
Ce–MCM-41-R-160[c]	29.4	1.02	15.5	1332
Ce–MCM-41-R-80	30.2	1.15	15.3	1242
Ce–MCM-41-R-40	31.1	1.14	15.4	1081
Ce–MCM-41-A-40	30.8	0.98	15.3	998
Ce–MCM-41-P-40	31.0	1.06	15.3	1062
Ce–MCM-41-R-20	31.8	0.91	15.3	983
Ce-Ex–MCM-41	27.1	0.98	16.8	1088
Ce-Im–MCM-41-20	28.4	0.92	15.5	1041
SiO_2–CeO_2-20	—	—	—	—

[a] R, A, and P denote samples synthesized under reflux conditions with stirring, in an autoclave under static conditions, and in a Parr autoclave with stirring, respectively.

[b] FWT, framework thickness = a_0 − pore diameter.

[c] Numbers denote Si/Ce molar ratio in gel.

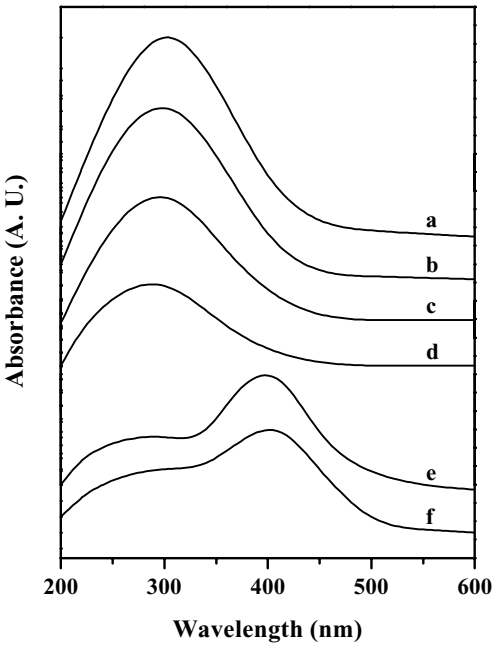

FIG. 3. Diffuse reflectance UV-vis spectra of calcined (a) Ce–MCM-41-R-20, (b) Ce–MCM-41-R-40, (c) Ce–MCM-41-R-80, (d) Ce–MCM-41-R-160, (e) Ce-exchanged MCM-41-20, and (f) SiO_2–CeO_2-20.

show a single peak with a maximum at ca. 300 nm and also its intensity increases with an increase in the Ce content of the samples. However, the diffuse reflectance UV–vis spectra of a silica and ceric oxide mixture (Si/Ce = 20) and of Ce-exchanged MCM-41 samples show two distinct bands, a small absorption at ca. 300 nm and a large absorption at ca. 400 nm.

The position of ligand to metal charge transfer ($O^{2-} \rightarrow Ce^{4+}$) spectra depends on the ligand field symmetry surrounding the Ce center. The electronic transitions from oxygen to cerium require higher energy for a tetra-coordinated Ce^{4+} than for a hexa-coordinated one. Therefore, it may be inferred that the absorption band centered at 300 nm for Ce–MCM-41 samples is due to the presence of one type of well-dispersed Ce^{4+} species (presumably in a tetra-coordinated environment), whereas in the case of a silica and ceric oxide mixture and Ce-exchanged MCM-41 samples, two distinct bands, at 300 and 400 nm, corresponds to two different types of Ce^{4+} species. The absorption at higher wavelength (~400 nm) may be assigned to hexa-coordinated Ce^{4+} species.

FTIR Spectroscopy

The IR spectra in the framework and the hydroxyl region of purely siliceous and different Ce-containing MCM-41 samples show bands characteristic of the MCM-41-type materials, as shown in Fig. 4. In the framework region (400–1300 cm^{-1}), the vibration band at ca. 1090 cm^{-1} is assigned to ν_{as}(Si–O–Si) and its wavenumber decreases with increasing incorporation of cerium in the structure. The wavenumber of this band decreases from 1090 cm^{-1} (for the Si–MCM-41 sample) to 1082 cm^{-1} (for Ce–MCM-41-R-20 sample). In general, this shift toward the lower wavenumber is considered an indication of the incorporation of Ce into the framework of MCM-41. Similarly, the band at ca. 970 cm^{-1}, observed for the Ce–MCM-41 samples, can be assigned to a ν_{as}(Si–O–Ce) vibration present in the framework of MCM-41. However, a band at ca. 962 cm^{-1} is also observed in the Si–MCM-41 sample. This band has been assigned to the Si–O stretching vibrations of $Si–O^- R^+$ groups, as $R^+ = H^+$ in the calcined state (20). Therefore, this band cannot be taken as proof of cerium incorporation in the case of MCM-41, because a large number of silanol groups are always present in the calcined Si–MCM-41 (21). Nevertheless, it has been observed that the band at ca. 962 cm^{-1} (in Si–MCM-41) is shifted toward the higher wavenumber side (970 cm^{-1}) in the case of Ce-containing MCM-41 samples. It has also been observed that the ν_{as}(Si–O–Ce) and/or ν(Si–OH) band intensity increases with respect to that of the ν_{as}(Si–O–Si) and/or ν(Si–OH) band when Ce content increases. This is generally taken as proof of the incorporation of metal into the framework of microporous and mesoporous metallosilicates (especially for microporous molecular sieves) (22). It may be demonstrated that the absorption at 970 cm^{-1} is essentially due to the increased degeneracy of the elongation vibration in the tetrahedral structure of SiO_4 induced by the change

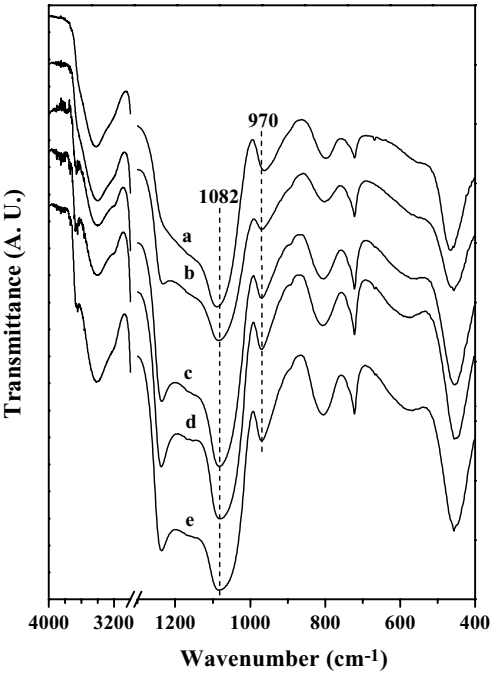

FIG. 4. IR spectra in the framework and the hydroxyl vibration region of calcined (a) Si–MCM-41, (b) Ce–MCM-41-R-160, (c) Ce–MCM-41-R-80, (d) Ce–MCM-41-R-40, and (e) Ce–MCM-41-R-20.

in the polarity of the Ce–O bond when Si is linked to Ce. The SiOH group formed by the hydrolysis of the Ce–O–Si bonds and the sharing of OH with Ce is then responsible for the absorption at higher wavenumbers compared to ordinary Si–OH groups (23). The lattice band ν_s(Si–O–Si) is also observed at ca. 802 and 804 cm^{-1} for Si–MCM-41 and Ce–MCM-41-R-20 samples (Figs. 4a and 4e), respectively. However, the small displacement (2 cm^{-1}) toward the higher wavenumber from sample a to e in Fig. 4 cannot be taken as proof of Ce incorporation, because this shift is within the spectral resolution of ±2 cm^{-1}.

In the hydroxyl region (3000–4000 cm^{-1}), the broad band centered at ca. 3422 cm^{-1} is observed for Si–MCM-41 whereas the same is shifted toward the lower wavenumber (15 cm^{-1}) and is observed at ca. 3407 cm^{-1} for all Ce–MCM-41 samples. A weak band at ca. 3661 cm^{-1} is also observed for Ce–MCM-41 samples. However, this band is not observed in the Si–MCM-41 sample. Both bands were assigned to silanol group vibrations situated inside the channels of MCM-41. The bands at 3422 and 3407 cm^{-1} result from silanol groups interacting via hydrogen bonding, whereas the other band, at 3661 cm^{-1}, is due to isolated silanol groups not interacting with each other via hydrogen bonding. The band shift from 3422 to 3407 cm^{-1} for Ce–MCM-41 samples compared to Si–MCM-41 may be assumed to be attributable to more hydrogen bonding in the Ce–MCM-41 samples due to the presence of more defect sites (SiOH groups). The band assignments for the IR spectra of Si–MCM-41 and Ce–MCM-41-R-20 are given in Table 3.

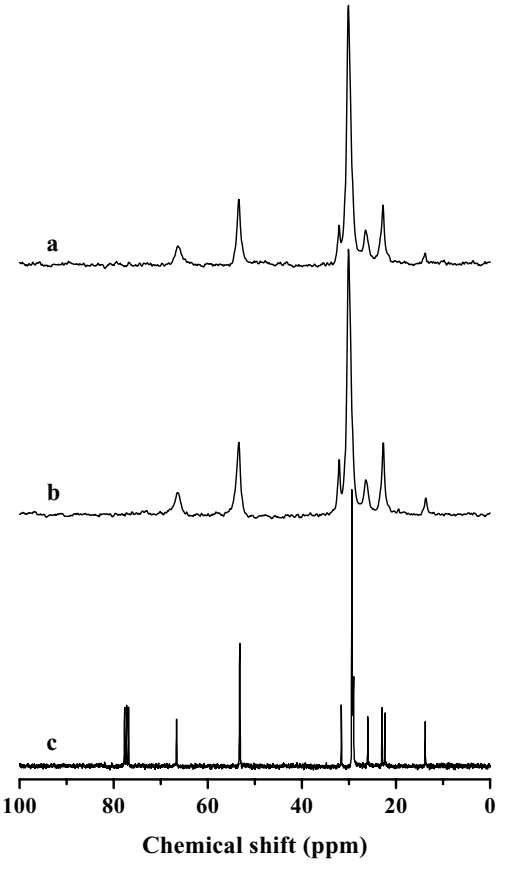

FIG. 5. ^{13}C CP MAS NMR spectra of as-synthesized (a) Ce–MCM-41-R (40), (b) Si–MCM-41, and (c) $CTMA^+$ ions in solution ($CDCl_3$).

^{13}C CP MAS NMR

The solid state ^{13}C CP MAS NMR spectra of as-synthesized Ce–MCM-41-R-40, Si–MCM-41, and $CTMA^+$ ions in solution ($CDCl_3$) are shown in Fig. 5. A comparison of the three spectra shows the incorporation of intact $CTMA^+$ cations inside the pores of the MCM-41 channels. All three ^{13}C NMR spectra are similar and therefore the peak assignments are also the same. The peaks at ca. 66 ppm in the spectra can be assigned to the CH_2 group of the cetyl chain that is neighbor to the nitrogen atom. The peaks at ca. 53 ppm can be assigned to the three CH_3 groups bonded to the nitrogen atom, whereas the resonances between 32 and 22 ppm are due to different CH_2 carbon atoms of the cetyl chain. The peaks observed at ca. 14 ppm can be attributed to the terminal CH_3 group of the cetyl chain. The peaks (triplet) at ca. 77 ppm for $CTMA^+$ in solution are due to solvent ($CDCl_3$).

A peak broadening is observed for the Ce–MCM-41 (Fig. 5, curve a) and Si–MCM-41 (curve b) in comparison with that in the case of the CTMA solution (curve c). The broadening of these peaks is generally attributed to the restricted translation movement of the organic molecules in the confined space. However, no peak broadening is observed for the Ce–MCM-41 samples compared to Si–MCM-41, especially for the peaks at ca. 66 and 53 ppm, which are generally attributed to the interaction of the template cations, with the negative charge on the framework induced by the incorporation of the di- and trivalent metal ions (13). This supports the incorporation of tetravalent cerium cations into the framework, which does not lead to any negative charge in the framework.

TABLE 3

Band Assignments in the IR Spectra of Si–MCM-41 and Ce–MCM-41-*R*-20

Wavenumber (cm^{-1})	Bond assignment for Si–MCM-41	Wavenumber (cm^{-1})	Bond assignment for Ce–MCM-41-*R*-20
3422	ν_{OH}(Si–O–H)	3661, 3407	ν_{OH}(Si–O–H)
1633	$\delta_{OH}(H_2O)$	1626	$\delta_{OH}(H_2O)$
1090	ν_{as}(Si–O–Si)	1082, 1234	ν_{as}(Si–O–Si)
962	ν_{as}(Si–O–Si) and/or ν(Si–OH)	970	ν_{as}(Si–O–Ce) and/or ν(Si–OH)
802, 721	ν_s(Si–O–Si)	804, 721	ν_s(Si–O–Si)
464	δ(Si–O–Si)	457	δ(Si–O–Si)

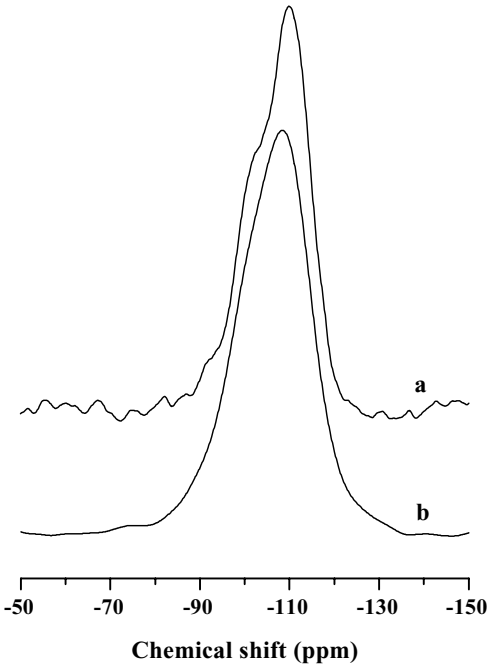

FIG. 6. ^{29}Si MAS NMR spectra of calcined (a) Ce–MCM-41-R-40 and (b) Si–MCM-41.

^{29}Si MAS NMR

Although, the ^{29}Si MAS NMR spectroscopy is a very sensitive probe for the characterization and identification of crystalline microporous zeolites and metallosilicates, in MCM-41, which is an ordered array of amorphous material, the observed peaks are broad due to the flexibility and broad range of T–O–T angles in the pore walls. The ^{29}Si MAS NMR spectra of the calcined Ce–MCM-41-R-40 sample, as shown in Fig. 6a, shows characteristic peaks at around −91, −102, and −110 ppm, which are usually assigned to Q_2, Q_3, and Q_4 species, respectively. However, the peaks for Q_2 and Q_3 species are not observed distinctly for the calcined Si–MCM-41 sample (Fig. 6b). Instead, a broad peak centered at −108.5 ppm (Q_4 species) is observed. It can be assumed that the presence of defect sites, generated by Q_2 and Q_3 species [$(–O–)_2Si(OH)_2$ and $(–O–)_3Si(OH)$ groups] in the Ce–MCM-41 samples, may provide mild acidic sites along with the CeOH groups.

SEM and EDX

The particle size and morphology of Si–MCM-41 and different Ce–MCM-41 samples were determined by scanning electron microscopy. The particle morphology of the samples is variable, but it is possible to obtain two types of discrete, differently shaped particles. The SEM micrographs of Ce–MCM-41-R-40 sample, as shown in Fig. 7, are typical of MCM-41-type materials exhibiting two different kinds of particle morphology. One is hexagonal and other one is a winding worm type (13). The hexagonal particles are of two types: (i) well-formed, relatively bigger particles of ca. 2 μm, and (ii) smaller particles ca. 0.5 μm in size. The unique hexagonal rod-type particle is also observed for the first time, as shown in Fig. 7, indicative of long-range ordering of Ce–MCM-41 samples. The worm-type particles may be formed due to the stirred synthesis, in contrast to the conventional static autoclave synthesis.

The energy dispersive X-ray analysis (EDX) for Si and Ce of the Ce–MCM-41 samples is given in Table 1. The

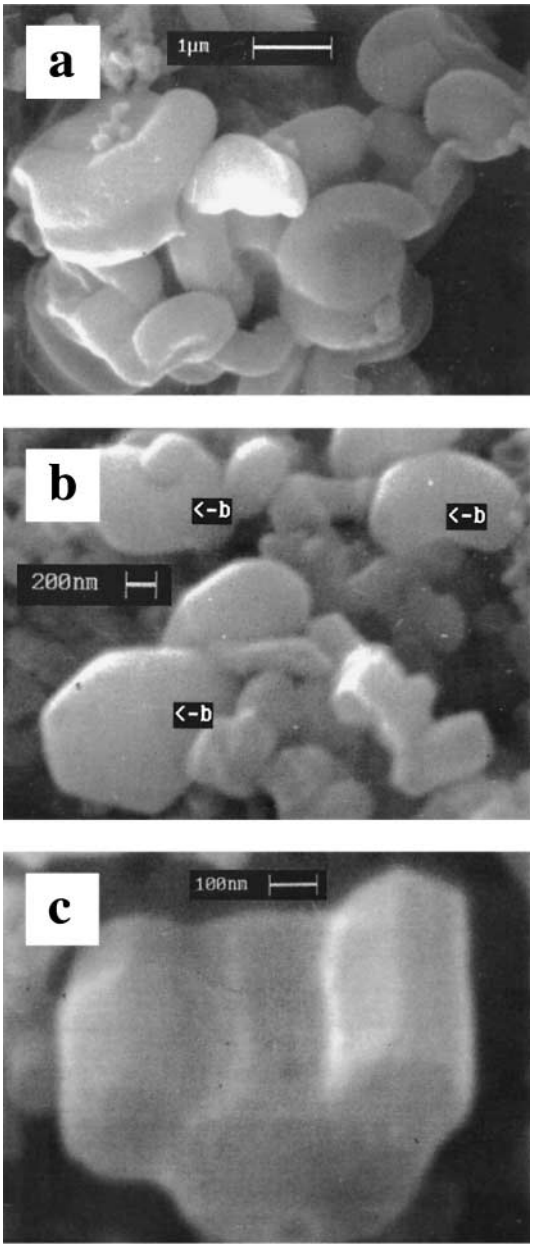

FIG. 7. Scanning electron micrographs of a calcined Ce–MCM-41-R-40 sample having different types of particle morphology: (a) winding worm type, (b) hexagonal type, and (c) unique hexagonal rod type.

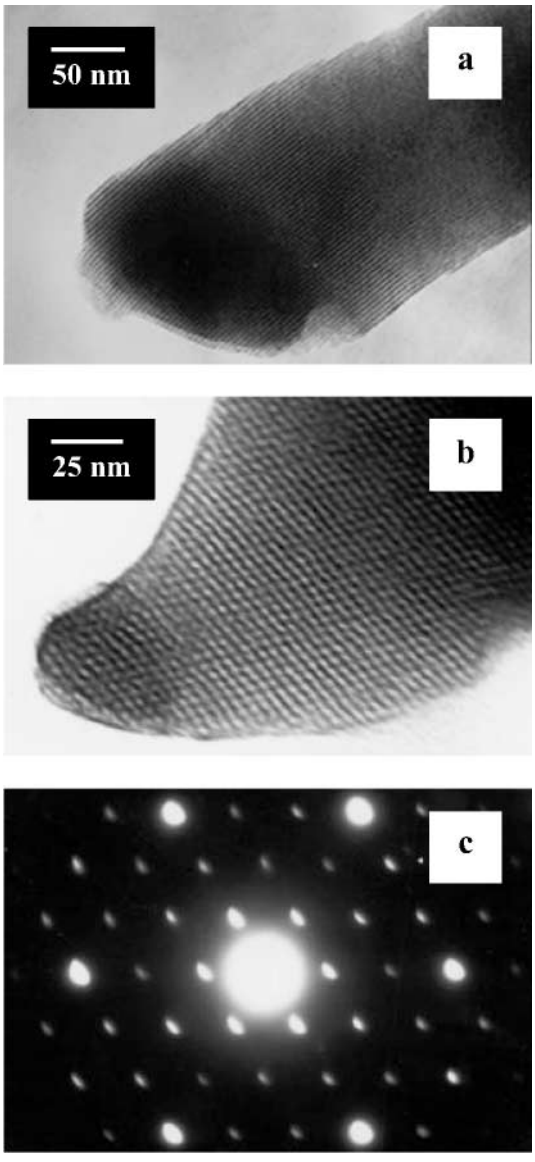

FIG. 8. Transmission electron micrographs of a calcined Ce–MCM-41-R-80 sample: (a) parallel fringes (side-on view), (b) hexagonal array (viewed along the pore direction), and (c) selected-area electron diffraction pattern of (b).

Si/Ce ratios of the gels and the calcined Ce–MCM-41 samples do not differ significantly, which indicates quite high efficiency for the incorporation of well-dispersed cerium into the framework and/or walls of the silica matrix of MCM-41.

TEM

Transmission electron microscopy (TEM) reveals parallel fringes corresponding to the side-on view of the long pores as well as a hexagonal system of lattice fringes along the pore direction, as shown in Figs. 8a and 8b, respectively. The equidistant parallel fringes of the Ce–MCM-41-R-80 sample (Fig. 8a) show the unique feature of separate layers and the addition of such layers, one after one, resulting in the formation of a bunch of layers. Therefore, it supports the idea that the formation of MCM-41 begins with the deposition of two to three monolayers of silicate precursor onto isolated surfactant micellar rods. Subsequently, these silicate-encapsulated composite species spontaneously form the long-range order characteristic of MCM-41 (2, 24). The pore size, d_{100} value, and framework thickness of each hexagonal array, shown in Fig. 8b for the Ce–MCM-41-R-80 sample, were measured and found to be ≈30, ≈40, and ≈7 Å, respectively. Therefore, the values of parameters obtained from the TEM measurements are approximately equal to those presented in Tables 1 and 2. A representative area electron diffraction pattern, shown in Fig. 8c, also exhibits well-defined hexagonal maxima and confirms the periodicity of the structure.

TGA–DTA

Thermogravimetric and differential thermal analyses (DTA) of Si–MCM-41 and Ce–MCM-41 samples were carried out under the same experimental conditions. The thermal patterns of the samples are qualitatively very similar. The total weight losses are 38 and 41 wt% for the Si–MCM-41 and Ce–MCM-41-R-40, respectively, as shown in Figs. 9a and 9b. The TGA–DTA curves of the two samples reveal that nearly all the template, including the water formed due to condensation of silanol groups, is lost from the pore system at a temperature of ∼600°C. The TGA curves of the two samples show five steps of weight loss. The steps can

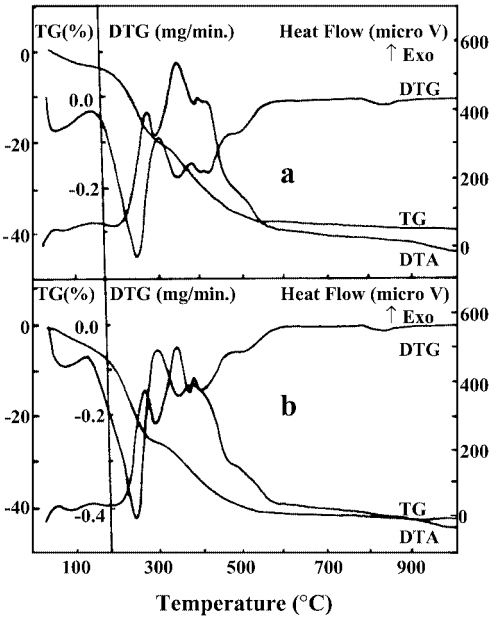

FIG. 9. TGA–DTA curves of as-synthesized (a) Si–MCM-41 and (b) Ce–MCM-41-R (40).

be distinguished as 35–130, 130–300, 300–380, 380–480, and 480–600°C. The weight loss for both the samples is ~4.0% in the first step and is due to desorption of physisorbed water held in the pores. The weight losses in the second (~20.0%) and third (~7.0%) steps are mainly associated with oxidative decomposition of templates. In the fourth step, the weight loss (~7.0%) is due to removal of coke formed in the previous steps by the decomposition of templates. In the last step, the weight loss (~2.0%) is mainly due to water loss formed by the condensation of silanol groups. It can be noticed that the weight losses of both Si–MCM-41 and Ce–MCM-41-R-40 samples are similar, indicative of similar pore filling of Ce–MCM-41 vis-à-vis Si–MCM-41 samples. The higher amount of weight loss for Ce–MCM-41-R-40 (41 wt%) than Si–MCM-41 (38 wt%) may be due to the bigger pore size of the Ce–MCM-41-R-40 sample.

Catalysis

The dehydration of cyclohexanol was carried out using different Ce–MCM-41 samples, as shown in Fig. 10. Ce-exchanged MCM-41, Ce-impregnated MCM-41, and silica–ceria catalysts were also used simultaneously to compare the catalytic results. It is observed that the cyclohexanol conversion is less in the presence of Ce-Ex–MCM-41, Ce-Im–MCM-41, and silica–ceria catalysts than the corresponding Ce–MCM-41 sample with same Si/Ce ratio. It has also been observed that as the Ce content increases in the Ce–MCM-41 samples, cyclohexanol conversion increases and reaches a maximum of ~16% conversion for the Ce–MCM-41-R-40 sample. However, further increase in the Ce content of Ce–MCM-41 samples does not increase the conversion; instead it decreases a little bit. A comparison of Ce–MCM-41-40 samples prepared by three different methods (R, A, and P) also shows that the Ce–MCM-41-R-40 sample is most active, whereas Ce–MCM-41-A-40 is the least active.

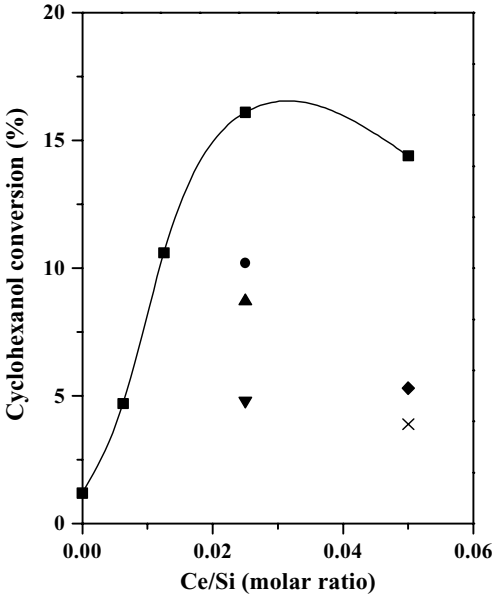

FIG. 10. Activity of Ce–MCM-41 samples in the dehydration of cyclohexanol to cyclohexene. (■) Si/Ce–MCM-41-R, (●) Ce–MCM-41-P-40, (▲) Ce–MCM-41-A-40, (▼) Ce-Ex–MCM-41, (◆) Ce-Im–MCM-41, and (×) SiO_2–CeO_2.

The Ce–MCM-41 samples possess selective oxidation properties in the presence of peroxides (aqueous H_2O_2 and TBHP) as oxidants. The hydroxylation of 1-naphthol was carried out using different Ce–MCM-41 samples. For comparison, the reactions were also carried out over Si–MCM-41, Ce-exchanged (Ce-Ex) MCM-41, Ce-impregnated (Ce-Im) MCM-41, and SiO_2–CeO_2 samples. The results show that Si–MCM-41 is inactive, whereas Ce-Ex–MCM-41,

TABLE 4

Activity of the Samples in the Hydroxylation of 1-Naphthol with H_2O_2[a]

Sample	1-Naphthol conversion (%)	H_2O_2 selectivity (%)	TOF (S^{-1})[b] × 10^4	Product distribution (%)[c]			
				1,2-DHN	1,4-DHN	1,2-NQ	1,4-NQ
Si–MCM-41		No detectable activity					
Ce–MCM-41-R-160	5.2	9.7	1.90	3.7	9.6	1.7	85.0
Ce–MCM-41-R-80	6.6	12.2	1.23	4.3	11.5	1.4	82.8
Ce–MCM-41-R-40	8.9	16.3	0.86	4.5	12.7	1.2	81.6
Ce–MCM-41-A-40	7.2	13.1	0.70	4.5	12.9	1.0	81.6
Ce–MCM-41-P-40	7.5	13.7	0.72	4.6	12.7	1.3	81.4
Ce–MCM-41-R-20	9.0	16.3	0.46	4.7	13.7	0.9	80.7
Ce-Ex–MCM-41	1.4	2.2	0.07	14.4	25.3	0.8	59.5
Ce-Im–MCM-41-20	1.1	1.7	0.05	15.1	26.7	0.5	57.7
SiO_2–CeO_2-20	1.0	1.6	0.05	16.2	28.5	0.4	54.9

[a] Reaction conditions: 1-naphthol = 1.44 g; 1-naphthol/H_2O_2 (mol/mol) = 4; catalyst = 20 wt% of the substrate (1-naphthol); solvent (acetonitrile)/1-naphthol (wt/wt) = 5; temperature = 353 K; reaction time = 12 h.

[b] Turnover frequency (TOF) = moles of H_2O_2 converted for producing products per mole of Ce per second.

[c] 1,2-DHN = 1,2-dihydroxynaphthalene; 1,4-DHN = 1,4-dihydroxynaphthalene; 1,2-NQ = 1,2-napthoquione; and 1,4-NQ = 1,4-naphthoquione.

TABLE 5

Activity of the Samples in the Hydroxylation of 1-Naphthol with *tert*-Butyl Hydroperoxide (TBHP)[a]

Sample	1-Naphthol conversion (%)	TBHP selectivity (%)	TOF (S^{-1})[b] × 10^4	Product distribution (%)[c]			
				1,2-DHN	1,4-DHN	1,2-NQ	1,4-NQ
Si–MCM-41	No detectable activity						
Ce–MCM-41-R-160	5.5	10.1	1.97	3.8	12.9	1.6	81.7
Ce–MCM-41-R-80	7.1	12.9	1.30	4.2	14.5	1.3	80.0
Ce–MCM-41-R-40	9.7	17.4	0.93	4.7	15.8	1.1	78.4
Ce–MCM-41-A-40	8.2	14.8	0.79	4.6	15.5	1.2	78.7
Ce–MCM-41-P-40	8.6	15.4	0.81	4.8	15.9	1.0	78.3
Ce–MCM-41-R-20	9.8	17.5	0.46	5.2	16.7	0.9	77.2
Ce-Ex–MCM-41	2.1	3.3	0.12	14.6	25.6	0.6	59.2
Ce-Im–MCM-41-20	1.8	2.8	0.07	15.4	27.0	0.5	57.1
SiO_2–CeO_2-20	1.4	2.2	0.05	16.1	26.8	0.4	56.7

[a] Reaction conditions: 1-naphthol = 1.44 g; 1-naphthol/TBHP (mol/mol) = 4; catalyst = 20 wt% of the substrate (1-naphthol); solvent (acetonitrile)/1-naphthol (wt/wt) = 5; temperature = 353 K; reaction time = 12 h.

[b] Turnover frequency (TOF) = moles of H_2O_2 converted for producing products per mole of Ce per second.

[c] 1,2-DHN = 1,2-dihydroxynaphthalene; 1,4-DHN = 1, 4-dihydroxynaphthalene; 1,2-NQ = 1,2-napthoquione; and 1,4-NQ = 1,4-naphthoquione.

Ce-Im–MCM-41, and SiO_2–CeO_2 are less active than the corresponding Ce–MCM-41 samples. The inactivity of the Si–MCM-41 sample suggests that Ce^{4+} ions are responsible for the activity. This is also confirmed by an increasing trend in the conversion of 1-naphthol with an increase in Ce content of the Ce–MCM-41 samples (Tables 4 and 5). However, the higher activity of Ce–MCM-41 than the corresponding Ce-Ex–MCM-41, Ce-Im–MCM-41, and SiO_2–CeO_2 samples may be attributable to the presence of tetra-coordinated Ce^{4+} ions presumably being in the framework of Ce–MCM-41 rather than in that of the Ce-Ex–MCM-41, Ce-Im–MCM-41, and SiO_2–CeO_2 samples. It has been observed that 1-naphthol conversion as well as peroxide selectivity is slightly higher for TBHP than H_2O_2. The major product in the hydroxylation of 1-naphthol, using both H_2O_2 and TBHP, is 1,4-naphthoquionone. The naphthoquinone derivatives are formed from the subsequent oxidation of corresponding dihydroxynaphthalene derivatives.

However, turnover frequency (TOF), both in the case of H_2O_2 and TBHP as oxidant, decreases with increasing Ce content in various Ce–MCM-41 samples, indicating that not all the Ce atoms are available for catalysis. This is common observation in the case of metal-incorporated MCM-41 and is correlated to the presence of heterometal ions inside the amorphous walls and thereby not accessible for reactants (25).

CONCLUSIONS

Ce–MCM-41 samples were prepared hydrothermally using different synthetic procedures. All the samples have very high surface area ($\geq$1000 m^2 g^{-1}) with a pore size of ~30 Å. Evidence for the presence of Ce in the framework and/or walls of the silica matrix were obtained from powder X-ray diffraction, N_2 adsorption, diffuse reflectance UV–vis spectra, and FTIR spectroscopic techniques. The absence of significant broadening of the ^{13}C signal of the CH_3 and CH_2 groups attached to N of the surfactant reveals the absence of a charged framework, suggesting the incorporation of Ce in its +4 oxidation state. Further, all the Ce–MCM-41 samples are EPR (electron paramagnetic resonance) inactive, indicating the incorporation of Ce as Ce^{4+} ions and not as Ce^{3+} ions. Ce–MCM-41 samples are active as catalysts, and higher activity for the dehydration of cyclohexanol and hydroxylation of 1-naphthol, in comparison to Ce-Ex–MCM-41, Ce-Im–MCM-41, and SiO_2–CeO_2 samples, is indicative of the presence of tetra-coordinated Ce in Si-rich environments.

ACKNOWLEDGMENTS

The authors are thankful to Drs. C. Gopinathan, M. Bhadbhade, R. Parischa, R. Gonnade, P. Rajmohanan, and N. Jacob for their helpful cooperation in characterizing the samples. S.C.L. thanks the Council of Scientific and Industrial Research, India, for granting him a research fellowship.

REFERENCES

1. Kresge, C. T., Leonowicz, M. E., Roth, W. J., Vartulli, J. C., and Beck, J. S., *Nature* **359**, 710 (1992).
2. Beck, J. S., Vartulli, J. C., Roth, W. J., Leonowicz, M. E., Kresge, C. T., Schmitt, K. D., Chu, C. T.-W., Olson, D. H., Sheppard, E. W., McCullen, S. B., Higgins, J. B., and Schlenker, J. L., *J. Am. Chem. Soc.* **114**, 10834 (1992).
3. Tanev, P. T., and Pinnavaia, T. J., *Science* **267**, 865 (1995).
4. Zhao, D., Luan, Z., and Kevan, L., *Chem. Commun*. 1009 (1997).
5. Jiménez, J. J., Torres, P. M., Pastor, P. O., Castellón, E. R., López, A. J., Jones, D. J., and Rozière, J., *Adv. Mater*. **10**, 812 (1998).

6. Jones, D. J., Aptel, G., Brandhorst, M., Jacquin, M., Jiménez-Jiménez, J., Jiménez-López, A., Maireles-Torres, P., Piwonski, I., Rodriguez-Castellón, E., Zajac, J., and Rozière, J., *J. Mater. Chem.* **10**, 1957 (2000).
7. Inagaki, S., Fukushima, Y., and Kuroda, K., *J. Chem. Soc. Chem. Commun*. 680 (1993).
8. Ryoo, R., Kim, J. M., Shin, C. H., and Lee, J. Y., *Stud. Surf. Sci. Catal*. **105**, 45 (1997).
9. Sayari, A., *Chem. Mater.* **8**, 1840 (1996).
10. Stucky, G. D., Huo, Q., Firouzi, A., Chmelka, B. F., Schacht, S., Martin, I. G. V., and Schüth, F., *Stud. Surf. Sci. Catal*. **105**, 3 (1997).
11. Corma, A., *Chem. Rev.* **97**, 2373 (1997).
12. Ying, J. Y., Mehnert, C. P., and Wong, M. S., *Angew. Chem. Int. Ed*. **38**, 56 (1999).
13. Carvalho, W. A., Varaldo, P. B., Wallau, M., and Schuchardt, U., *Zeolites* **18**, 408 (1997) and references therein.
14. Guo, H., Wang, X., and Zou, B., *Cuihua Xuebao* **18**, 185 (1997).
15. Chen, X., Huang, L., and Li, Q., *J. Phys. Chem. B* **101**, 8460 (1997).
16. Luan, Z., He, H., Zhou, W., Cheng, C. F., and Klinowski, J., *J. Chem. Soc., Faraday Trans*. **91**, 2955 (1995).
17. Kruk, M., Jaroniec, M., and Sayari, A., *Langmuir* **13**, 6267 (1997).
18. Zhang, W., Fröba, M., Wang, J., Tanev, P. T., Wong, J., and Pinnavaia, T. J., *J. Am. Chem. Soc.* **118**, 9164 (1996).
19. Chaudhari, K., Das, T. K., Rajmohanan, P. R., Lazar, K., Sivasanker, S., and Chandwadkar, A. J., *J. Catal.* **183**, 281 (1999).
20. Decottiguies, M., Phalippou, J., and Zarzycki, J., *J. Mater. Sci*. **13**, 2605 (1978).
21. Kolodziejski, W., Corma, A., Navarro, M. T., and Pariente, J. P., *Solid State Nucl. Magn. Reson*. **2**, 253 (1993).
22. Boccuti, M. R., Rao, K. M., Zecchina, A., Leofanti, G., and Petrini, G., *Stud. Surf. Sci. Catal*. **48**, 133 (1989).
23. Alba, M. D., Luan, Z., and Klinowski, J., *J. Phys. Chem. B* **100**, 2178 (1996).
24. Chen, C.-Y., Burkett, S. L., Li, H.-X., and Davis, M. E., *Microporous Mater*. **2**, 27 (1993).
25. Blasco, T., Corma, A., Navarro, M. T., and Pariente, J. P., *J. Catal.* **156**, 65 (1995).